


Interplay of valley selection and helicity exchange of light in Raman scattering for graphene and MoS₂

Yuki Tatsumi* and Riichiro Saito

Department of Physics, Tohoku University, Sendai 980-8578, Japan
 (Received 9 November 2017; revised manuscript received 23 January 2018; published 8 March 2018)

Raman spectra of graphene and MoS₂ are calculated for incident and scattered circularly polarized light. In the case of graphene, the well known *G*-band Raman spectra have a not well known property that the helicity of the incident circularly polarized light changes to another helicity in the scattered light. Using the electron-photon and electron-phonon matrix elements by first-principles calculation, we calculate resonant Raman spectra of graphene and MoS₂ for circularly polarized light which are compared with recent experiments. The Raman intensity for circularly polarized light is relevant to optical valley polarization in the case of MoS₂. We also discuss how the helicity-selection rule can be modified by applying stress to graphene.

DOI: [10.1103/PhysRevB.97.115407](https://doi.org/10.1103/PhysRevB.97.115407)

I. INTRODUCTION

After successful mechanical exfoliation of graphene [1], atomic layer materials have attracted a lot of interest in their unique electronic properties. In particular, for atomic layer materials with a hexagonal lattice such as graphene, hexagonal boron nitride (hBN), and transition-metal dichalcogenides (TMDs), two valleys exist, the so-called *K* and *K'* valleys at the corner of the hexagonal Brillouin zone. The hexagonal lattice with independent multivalleys is promising for valleytronic applications [2]. In particular, an optical way to realize valleytronics is by using circularly polarized light. The optical transition of the electrons excited by the left-handed (right-handed) circularly polarized light σ_+ (σ_-) occurs only at the *K'* (*K*) valley in materials without inversion symmetry such as hBN and TMDs [3,4], which is known as valley-selective optical transition. Here, the helicity of a photon σ is defined as an eigenvalue of \hat{S}_z given by $\hat{S}_z \mathbf{P}_\sigma = \hbar \sigma \mathbf{P}_\sigma$, where \hat{S}_z and \mathbf{P}_σ are the *z* component of the SO(3) rotational group and polarization vector for the circularly polarized light, respectively [5]. The integer eigenvalue $\sigma = +1$ (-1) corresponds to the left-(right-) handed circularly polarized light. The valley-selective optical transition (or, simply, valley polarization) is observed by photoluminescence [6–18], optical absorption accompanied by the optical Stark effect [19], and electroluminescence [20]. However, it is not always straightforward to apply optical valleytronics of atomic layer materials to optovalleytronic devices since we expect relaxation of the photoexcited carrier that breaks the information of the valleys. Nevertheless, Raman spectra can retain the information of the valleys since the inelastic scattered light in the first-order Raman spectra occurs without any relaxation except for emitting a phonon. In fact, the absorption and emission of a photon in the first-order Raman process occur within the same valley in which the effect of valley polarization is essential.

Raman spectroscopy is a nondestructive and noninvasive technique to characterize the properties of atomic layer mate-

rials [21–23]. The measured Raman spectra sensitively depend on the crystal structure, the phonon mode, incident laser energy, and the polarization of light, which is sufficient even for characterizing the stacking order of atomic layer materials [24,25]. In graphene, which does not have valley polarization, on the other hand, we can observe a strong Raman peak, the so-called *G* band, at around 1600 cm⁻¹ which originates from the degenerate in-plane transverse optical (iTO) and longitudinal optical (LO) phonon modes at the Γ point [21,22] [see Fig. 1(a)]. Drapcho *et al.* observed that the scattered circularly polarized light of the *G* band has a different helicity than that of the incident light [26]. Hereafter, we call this phenomenon helicity exchange. It is clear from the present paper that the helicity-exchange phenomenon itself is independent of valley polarization, even though both phenomena occur via the circularly polarized light. It is important to point out that the helicity-exchange phenomenon depends on the symmetry of phonon modes. In the case of TMDs, Chen *et al.* [27] reported that the helicity exchange of Raman spectra for the circularly polarized light occurs (does not occur) for the IMC (OC) phonon mode, whose peak appears at 390 (410) cm⁻¹ in monolayer MoS₂ [28–33]. Here, the IMC mode is the in-plane vibration of the transition-metal and chalcogen atoms, while the OC mode is the out-of-plane vibration of chalcogen atoms [see Fig. 1(b)]. Such helicity-dependent Raman scattering is observed for the shear and breathing interlayer modes [see Fig. 1(b)] in multilayer TMDs, too [27]. Since a Raman scattering process consists of the absorption or emission of a phonon, the helicity-exchange phenomenon for the IMC mode might imply that the IMC phonon takes and releases the angular momentum of the photon. The angular momentum of a phonon is defined by the phase difference between the in-plane *x* and *y* directions of the phonon eigenvector. Zhang and Niu discussed the angular momentum of phonons in the hexagonal lattice [34,35]. According to the formulation by Zhang and Niu [35], a nondegenerate Γ -point phonon such as the OC mode in TMDs cannot have angular momentum. Thus, such a Γ -point phonon cannot accept the angular momentum from the photon, which seems consistent with the fact that the helicity exchange does not occur for the OC mode. On the other hand,

*Corresponding author: tatsumi@flex.phys.tohoku.ac.jp

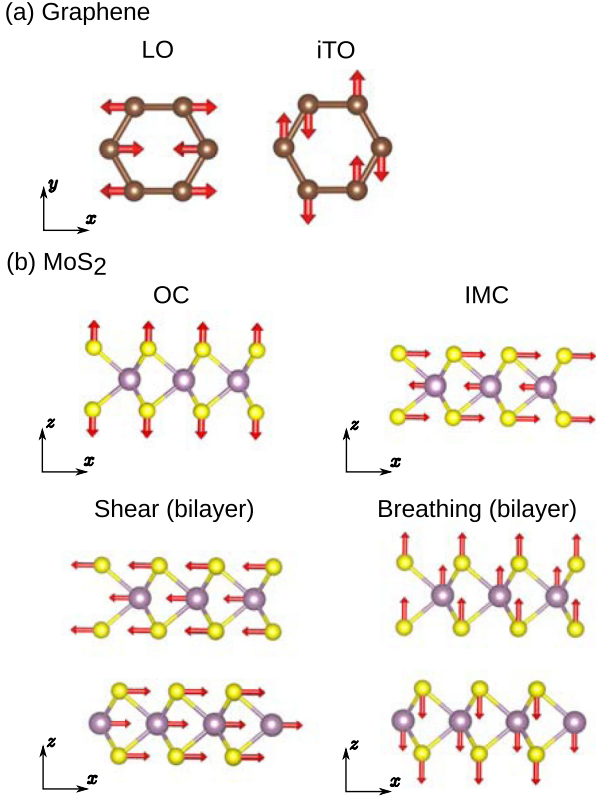


FIG. 1. Atomic vibrations of (a) the iTO and LO modes in graphene and (b) the OC, IMC, shear, and breathing modes in MoS₂. The shear and breathing modes are observed only in multilayer MoS₂.

degenerate phonon modes such as the G band of graphene or the IMC mode of TMDs can have angular momentum even at the Γ point by constructing the superposition of the degenerate eigenvectors [35]. Since the degeneracy of the phonon mode is essential to discuss the helicity-dependent Raman scattering, it is important to consider the helicity-exchange phenomenon of the Raman spectra for strained graphene in which the degeneracy of the G band is lifted to G^+ and G^- [36–38].

In this paper, we calculate the Raman spectra of the G band of graphene and the IMC and OC modes of mono- and bilayer MoS₂, for which we discuss the interplay of the valley polarization and the helicity-dependent Raman scattering. In order to discuss the relationship between the angular momentum of phonons for the degenerate phonon modes and the helicity-exchange phenomenon, we apply the uniaxial strain on the graphene to lift the degeneracy of the G band and calculate the Raman intensity of the G^+ and G^- bands for the circularly polarized light.

The organization of this paper is as follows. In Sec. II, we briefly explain the calculation of the helicity-dependent Raman spectra by first-principles calculation. In Sec. III A, we show calculated electronic structures and phonon modes of graphene and MoS₂. In Sec. III B, we show and discuss the calculated results of Raman spectra for graphene and MoS₂ for the circularly polarized light. In Sec. III C, we show the helicity-dependent Raman spectra of strained graphene to lift the degeneracy of the G -band phonon. Finally, in Sec. IV, we give a summary of the paper.

II. METHOD

A. Calculation of Raman intensity

The first-order resonant Raman intensity of the ν th phonon mode for the incident σ and scattered σ' circularly polarized light ($\sigma, \sigma' = \sigma_{\pm}$) is given by the time-dependent third-order perturbation theory as follows [39]:

$$I_{\sigma'\sigma}^{\nu}(E_L) \propto \left| \sum_{\mathbf{k}} \sum_{i(=f), m, m'} M_{\text{opt}}^{fm'\sigma'}(\mathbf{k}) M_{\text{ep}}^{m'm\nu}(\mathbf{k}) M_{\text{opt}}^{mi\sigma}(\mathbf{k}) \right|^2 \times \frac{1}{(E_L - \Delta E_{mi} - i\gamma)(E_L - \hbar\omega_{\nu} - \Delta E_{m'i} - i\gamma)}, \quad (1)$$

where E_L and $\hbar\omega_{\nu}$ denote the energies of the incident light and the ν th phonon, respectively. $M_{\text{opt}}^{fi\sigma}(\mathbf{k})$ and $M_{\text{ep}}^{fi\nu}(\mathbf{k})$ are, respectively, the electron-photon and electron-phonon matrix elements between the initial (i) and final (f) states for the given circularly polarized light σ or the ν th phonon. The parameter γ is the resonance window, which is related to the lifetime of the photoexcited carrier. Here, we adopt $\gamma = 0.1$ eV, which is estimated by the measurement of Raman excitation profile [40]. The energy of the scattered light E_s is given by $E_L - \hbar\omega_{\nu}$, and the Raman shift is defined by $E_{RS} = E_L - E_s$ (in units of cm^{-1}). In Raman spectra, Raman intensity is plotted as a function of E_{RS} , in which the intensity has a value only at each $E_{RS} = \hbar\omega_{\nu}$. In order to compare the calculated Raman spectra with the experiment that has a finite spectral width for each peak, we add the spectral width Γ for each peak by using a Lorentzian function $\frac{1}{\pi} \frac{\Gamma}{(E_{RS} - \hbar\omega_{\nu})^2 + \Gamma^2}$. Here, Γ is proportional to the inverse of the lifetime of the phonon. We adopt the broadening factor $\Gamma = 0.5$ meV for graphene and $\Gamma = 0.2$ meV for MoS₂ in this calculation to reproduce the spectral widths of Raman spectra in the experiment [26,27].

The electron-photon matrix element is calculated within the dipole approximation [41] as follows:

$$M_{\text{opt}}^{fi\sigma}(\mathbf{k}) \propto \mathbf{P}_{\sigma} \cdot \mathbf{D}^{fi}(\mathbf{k}), \quad (2)$$

where $\mathbf{D}^{fi}(\mathbf{k})$ is the dipole vector for the initial (i) and final (f) states that is expressed by [42]

$$\mathbf{D}^{fi}(\mathbf{k}) = \langle \psi^f(\mathbf{k}, \mathbf{r}) | \nabla | \psi^i(\mathbf{k}, \mathbf{r}) \rangle \quad (3)$$

and \mathbf{P}_{σ} in Eq. (2) is the Jones vector that expresses the polarization for σ_+ (σ_-) light, which is given by $\mathbf{P}_{\sigma_+} = (1, i, 0)$ [$\mathbf{P}_{\sigma_-} = (1, -i, 0)$]. The electron-phonon matrix element with a phonon of wave vector $\mathbf{q} = 0$ (Γ point phonon) is given by using the following formula [43,44]:

$$M_{\text{ep}}^{fi\nu}(\mathbf{k}) \propto \langle \psi^f(\mathbf{k}, \mathbf{r}) | \partial_{v, \mathbf{q}=0} V | \psi^i(\mathbf{k}, \mathbf{r}) \rangle, \quad (4)$$

where $\partial_{v, \mathbf{q}=0} V$ is the derivative of the self-consistent potential associated with a ν th Γ -point phonon [45].

The helicity-selection rule is simply discussed using the Raman tensor, which is the classical theory based on the symmetry of the phonon modes. The Raman intensity $I_{\sigma'\sigma}^{\nu}$ is calculated by a product of the polarization vectors of incident (\mathbf{P}_{σ}) and scattered ($\mathbf{P}_{\sigma'}$) light and a Raman tensor $\overleftrightarrow{\mathbf{R}}^{\nu}$ (ν) as follows:

$$I_{\sigma'\sigma}^{\nu} = |\mathbf{P}_{\sigma'}^* \cdot \overleftrightarrow{\mathbf{R}}^{\nu} \cdot \mathbf{P}_{\sigma}|^2. \quad (5)$$

TABLE I. Raman tensors and the Raman intensities calculated for the same (different) helicity $I_{\sigma+\sigma+}^v$ ($I_{\sigma-\sigma+}^v$) of incident and scattered light by Raman tensor [Eq. (5)] for the Raman active modes of D_{6h} (graphene), D_{3h} (monolayer MoS₂), D_{3d} (bilayer MoS₂), and D_{2h} (strained graphene).

Symmetry	Mode	$\overleftrightarrow{R}(\nu)$	$I_{\sigma+\sigma+}^v$	$I_{\sigma-\sigma+}^v$
D_{6h} (graphene)	E_{2g} (G band)	$\begin{pmatrix} 0 & d & 0 \\ d & 0 & 0 \\ 0 & 0 & 0 \end{pmatrix}, \begin{pmatrix} d & 0 & 0 \\ 0 & -d & 0 \\ 0 & 0 & 0 \end{pmatrix}$	0	$ d ^2$
	$A'_1(\text{OC}, D_{3h})$ $A_{1g}(\text{OC}, D_{3d})$	$\begin{pmatrix} a & 0 & 0 \\ 0 & a & 0 \\ 0 & 0 & c \end{pmatrix}$	$ a ^2$	0
D_{3h} (monolayer MoS ₂) D_{3d} (bilayer MoS ₂)	$E'_g(\text{IMC}, D_{3h})$ $E_g(\text{IMC}, D_{3d})$	$\begin{pmatrix} 0 & d & 0 \\ d & 0 & 0 \\ 0 & 0 & 0 \end{pmatrix}, \begin{pmatrix} d & 0 & 0 \\ 0 & -d & 0 \\ 0 & 0 & 0 \end{pmatrix}$	0	$ d ^2$
	A_g (G^-)	$\begin{pmatrix} a & 0 & 0 \\ 0 & b & 0 \\ 0 & 0 & c \end{pmatrix}$	$ \frac{a+b}{2} ^2$	$ \frac{a-b}{2} ^2$
D_{2h} (strained graphene)	B_{1g} (G^+)	$\begin{pmatrix} 0 & d & 0 \\ d & 0 & 0 \\ 0 & 0 & 0 \end{pmatrix}$	0	$ d ^2$

In Table I, we show the Raman tensors and the Raman intensity for symmetries of D_{6h} (graphene), D_{3h} (monolayer MoS₂), D_{3d} (bilayer MoS₂), and D_{2h} (strained graphene) for circularly polarized light given from Eq. (5). For graphene and monolayer MoS₂, the selection rule of helicity-dependent Raman spectra can be explained simply with the Raman tensor. However, the selection rule for the A_g mode in D_{2h} symmetry depends on the components a and b in the Raman tensor. This indicates that the helicity-selection rule for the A_g mode in D_{2h} symmetry should be calculated by numerical calculation. Comparing Eq. (5) with Eqs. (1) and (2), we obtain the formula for the Raman tensor with quantum-mechanical description as follows [23]:

$$\overleftrightarrow{R}(\nu) = \sum_k \sum_{i=f,m,m'} \frac{\mathbf{D}^{f m'}(\mathbf{k}) \cdot \mathbf{M}_{\text{ep},\nu}^{m' m}(\mathbf{k}) \cdot \mathbf{D}^{m i}(\mathbf{k})^*}{[E_L - E^{m i}(\mathbf{k}) - i\gamma][E_L - E^{m' i}(\mathbf{k}) - \hbar\omega_\nu - i\gamma]} \quad (6)$$

B. Computational details

1. Electron-photon interaction

In order to obtain the electron-photon interaction given in Eq. (2), we calculate the wave functions based on the first-principles density functional theory (DFT) calculation by using the QUANTUM ESPRESSO code [46]. All first-principles calculations in this paper are performed using the local-density approximation for the exchange-correlation functional with the norm-conserving pseudopotential. The wave function is described by the plane-wave basis employed by the cutoff energy of 25 Ry. We use a $10 \times 10 \times 1$ Monkhorst-Pack k mesh [47] to sample a Brillouin zone for self-consistent field (SCF) calculation. After the SCF calculation, we perform the non-self-consistent field calculation for a $51 \times 45 \times 1$ k mesh

without a Monkhorst-Pack mesh and obtain the wave functions for 2295 k points. To avoid the interlayer interaction for mono- and bilayer structures, we construct a supercell with a lattice parameter of $c_0/a_0 = 4$ (10) for graphene (MoS₂), where a_0 and c_0 are the lattice constants of the in-plane and out-of-plane directions, respectively.

2. Electron-phonon interaction

The phonon modes are calculated within the density functional perturbation theory [48]. We calculate the electron-phonon interaction by using the EPW code [43], which applies the maximally localized Wannier function combined with the phonon calculation at the Γ point from the QUANTUM ESPRESSO code. The converging parameter for the phonon calculation is stricter than the calculation for the electronic energy band. We use the cutoff energies of 600, 240, and 400 Ry with $32 \times 32 \times 1$, $42 \times 42 \times 1$, and $48 \times 48 \times 1$ Monkhorst-Pack k meshes for graphene and monolayer and bilayer MoS₂, respectively. From the EPW package, we extract the electron-phonon matrix elements for the Γ -point phonon for a $51 \times 45 \times 1$ k mesh in the first Brillouin zone and obtain the electron-phonon matrix elements for 2295 k points.

3. Calculation of Raman intensity

The resonant Raman intensity for the first-order scattering is calculated using Eq. (1). Since Eq. (1) becomes singular because of the energy denominators compared with the smooth function of the matrix elements, we add three points between each pair of k points in the $51 \times 45 \times 1$ mesh and linearly interpolate the matrix elements and energies on $201 \times 177 \times 1 = 35\,577$ k points. We also check the accuracy of the integration by comparing $401 \times 353 \times 1 = 141\,553$ k points.

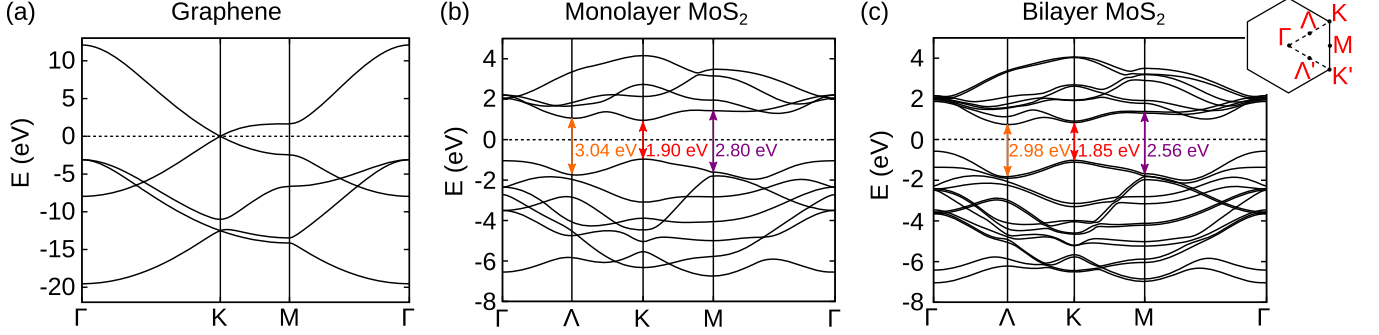


FIG. 2. Calculated electronic energy bands of (a) graphene, (b) monolayer, and (c) bilayer MoS₂. The inset in (c) is the first Brillouin zone of mono- and bilayer MoS₂.

III. RESULTS AND DISCUSSION

A. Electronic structure and phonon modes

In Figs. 2(a)–2(c), we show the electronic energy bands of graphene and monolayer and bilayer MoS₂, respectively. In the present calculation, we consider two π and three σ orbitals for graphene and 3 p orbitals of sulfur and 4 d orbitals of molybdenum for MoS₂. It is well known that the DFT calculation underestimates the value of the energy gap for the semiconductor. Thus, we upshift the conduction band of MoS₂ to reproduce the experimental energy band gap (1.90 eV) of monolayer MoS₂ estimated by the measurement of the optical absorption spectra [49].

TABLE II. Calculated phonon modes at the Γ point for graphene and monolayer (1L) and bilayer (2L) MoS₂. R (IR) denotes the Raman (infrared) active mode.

	Mode	ω_v (cm ⁻¹)	IR/R
Graphene (D_{6h})	A_{2u}	0	IR
	E_{1u}	0	IR
	B_{2g}	905.7	
	E_{2g} (iTO + LO)	1618.8	R
1L MoS ₂ (D_{3h})	A_2''	0	IR
	E_1'	0	IR+R
	E_1''	287.4	R
	E_1' (IMC)	388.5	IR+R
	A_1' (OC)	407.3	R
	A_2''	472.3	IR
2L MoS ₂ (D_{3d})	A_{2u}	0	IR
	E_u	0	IR
	E_g (shear)	21.9	R
	A_{1g} (breathing)	30.4	R
	E_u	286.7	IR
	E_g	288.7	R
	E_u	388.3	IR
	E_g (IMC)	388.9	R
	A_{2u}	406.6	IR
	A_{1g} (OC)	408.0	R
	A_{2u}	471.0	IR
	A_{1g}	472.6	R

In Table II, we show the calculated frequencies of the phonons at the Γ point which are relevant to the first-order Raman scattering. Only the Raman active modes of the Γ -point phonons with zero wave vector (or zone-center phonons) can be observed in the first-order Raman process to satisfy the conservation of momentum [23]. In this paper, we focus on the G band (LO and iTO modes) of graphene and the IMC, OC, shear, and breathing modes of MoS₂, where the eigenvectors of the phonons are illustrated in Figs. 1(a) and 1(b), respectively.

B. Helicity-dependent Raman spectra of graphene and MoS₂

In Fig. 3, we show the calculated Raman spectra of the G band of graphene [Fig. 3(a)] and the IMC and OC modes of mono- and bilayer MoS₂ [Fig. 3(b)] in the case of the same [$\bar{z}(\sigma_+ \sigma_+)z$, orange lines] and different [$\bar{z}(\sigma_+ \sigma_-)z$, blue lines] circularly polarized light for incident and scattered light, calculated using Eq. (1) combined with the Lorentzian function to express the spectral width. As shown in Fig. 3, the G band in graphene and the IMC peak in monolayer MoS₂ show nonzero Raman intensities for helicity-changing $\bar{z}(\sigma_+ \sigma_-)z$ scattering, while the OC peak has nonzero Raman intensity for helicity-conserving $\bar{z}(\sigma_+ \sigma_+)z$ scattering. This means that the G band of graphene and the IMC mode of MoS₂ show the helicity-exchange phenomenon, which is consistent with the experimental results by Drapcho *et al.* [26] and Chen *et al.* [27], respectively. However, as shown in Fig. 3(b), the Raman intensity of monolayer MoS₂ in helicity-dependent Raman spectra strongly depends on the incident laser energy E_L . This phenomenon occurs since the electron-photon matrix element depends on E_L [50]. Electron-photon and electron-phonon matrix elements for graphene and monolayer MoS₂ are shown in Figs. S1 and S2 of the Supplemental Material, respectively [51]. The values of the electron-photon and electron-phonon matrix elements depend on the laser energy, but the helicity-selection rule is determined by the symmetry of the matrix elements, which is also discussed using group theory in the Supplemental Material. We note that the helicity-selection rules given by group theory eventually follow directly from the form of the Raman tensors.

Let us discuss the relation between the valley polarization and the Raman intensity for the helicity-dependent Raman spectra. The contribution of valley polarization is clarified

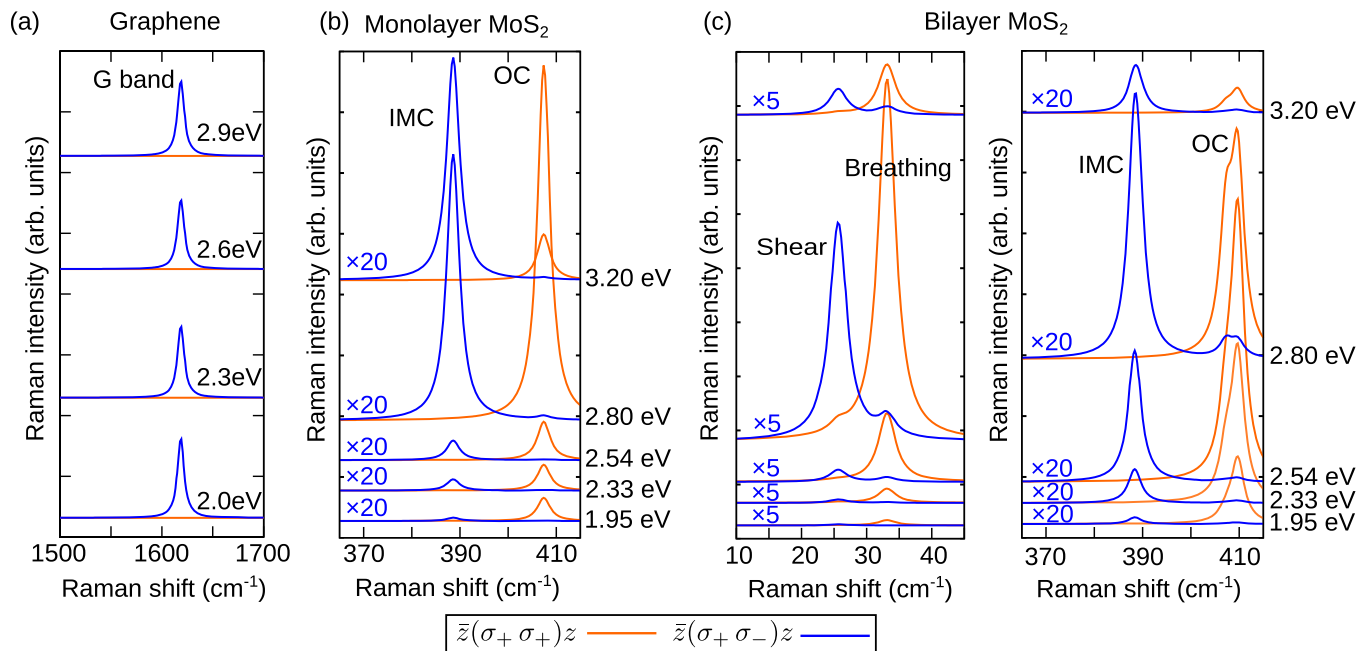


FIG. 3. Calculated helicity-dependent Raman spectra of (a) the G band in graphene, (b) the IMC (E') and OC (A'_1) modes in monolayer MoS_2 , and (c) the IMC, OC, shear, and breathing modes in bilayer MoS_2 . We show the Raman spectra for incident laser energy of 2.0, 2.3, 2.6, and 2.9 eV for graphene and 1.95, 2.33, 2.54, 2.80, and 3.20 eV for MoS_2 .

by considering the laser energy dependence of Raman peak intensity (the Raman excitation profile in the experiment). In Fig. 4, we show the laser energy dependence of the helicity-changing IMC and helicity-conserving OC Raman peak intensities for monolayer and bilayer MoS_2 . We also show the energy dependence of the degree of valley polarization ρ^K , which is defined by [50]

$$\rho^K = -\frac{I_{K,\sigma^+}^{\text{abs}} - I_{K,\sigma^-}^{\text{abs}}}{I_{K,\sigma^+}^{\text{abs}} + I_{K,\sigma^-}^{\text{abs}}}, \quad (7)$$

where $I_{K,\sigma^+}^{\text{abs}}$ and $I_{K,\sigma^-}^{\text{abs}}$ are the intensities of the optical absorption in the region around the K point for σ_+ and σ_- light, respectively. In Fig. 4(a), there are two energies to enhance the

Raman intensity. These two energies correspond to $E_L = 2.80$ and 3.20 eV, in which the optical transition occurs around the Λ [Λ' ; around the center of Γ - K (Γ - K') line] and the M (the center of the two hexagonal edges) points in the Brillouin zone [50], respectively, as shown in the inset of Fig. 2(c). We note that the energy gap at the M point in this calculation is 3.04 eV. However, the valley polarization becomes zero at $E_L = 3.10$ eV, which is a slightly higher energy than the energy gap at the M point, as shown in Fig. 4(a). As shown in Fig. 5, there is a conduction band minimum at the Λ (Λ') point, and it is known that strong optical absorption is observed in the region between Λ (Λ') and Γ by the nesting of the energy bands [52,53]. Thus, the Raman intensity at $E_L = 2.80$ eV is enhanced by

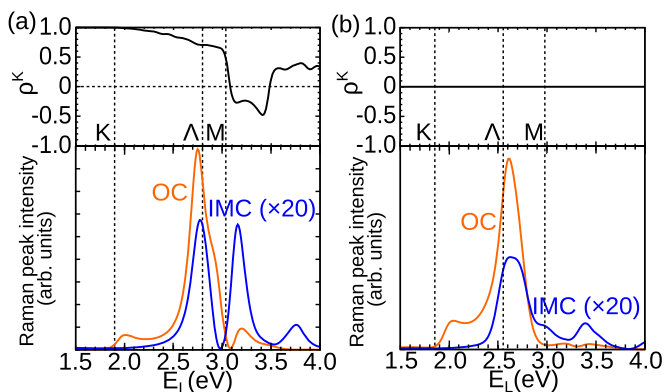


FIG. 4. Laser energy dependence of the degree of valley polarization ρ^K and the Raman peak intensity for helicity-changing IMC and the helicity-conserving OC modes of (a) monolayer and (b) bilayer MoS_2 . The energy gaps at the K , Λ , and M points are shown by dashed lines.

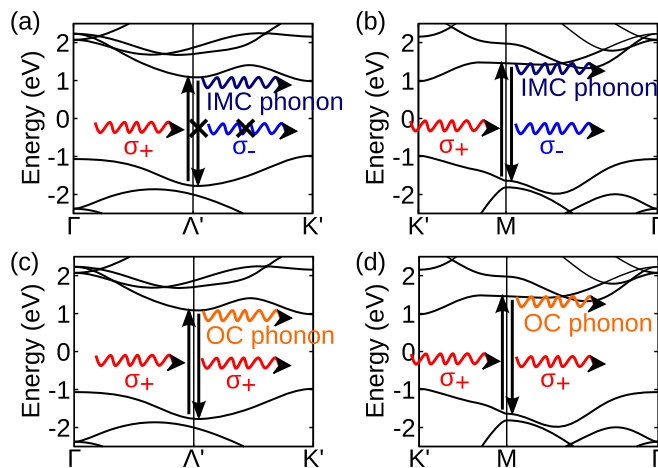


FIG. 5. The Raman scattering process of monolayer MoS_2 for (a) the IMC mode at the Λ' , (b) the IMC mode at the M , (c) the OC mode at the Λ' , and (d) the OC mode at the M .

the strong optical absorption and emission near the Λ (Λ') point. The optical absorption is also strong at the M point, but the Raman intensity of the OC mode is suppressed at $E_L = 3.20$ eV because of the contribution of the electron-phonon matrix element around the M point, whose amplitude is smaller than that around the Λ point [51] [see Fig. S2(b)]. For the IMC mode, the Raman peak intensity is comparable in the cases of $E_L = 2.80$ and 3.20 eV, which is explained by the valley polarization. That is, in monolayer TMDs, the σ_- (σ_+) light is absorbed only at the K (K') point, which is optical valley polarization. Such a valley-selective optical transition occurs also in the Λ (Λ') valley, which suppresses the Raman intensity of the helicity-changing IMC mode. However, in the case of $E_L = 3.20$ eV, in which there is low valley polarization, such suppression does not occur, which is the reason why the Raman intensity for the IMC mode becomes large for $E_L = 3.20$ eV. In Fig. 5, we illustrate this situation. Even though the helicity of the photon is changed in the case of the IMC mode, the optical emission process becomes forbidden by the valley-polarization effect for the photon emission [Fig. 5(a)]. On the other hand, since there is no valley polarization (σ_+ and σ_- light are equally absorbed) at the M point, the helicity-changing IMC Raman peak is not suppressed by the valley polarization at the M point [Fig. 5(b)]. Furthermore, since the helicity-conserving OC peak is not affected by the valley-polarization effect of the optical transition, the suppression of the Raman process by valley polarization does not occur [Figs. 5(c) and 5(d)]. We note that the optical valley polarization near the Λ (Λ') point is not 100% ($\sim 80\%$) and the IMC Raman peak is eventually enhanced by the nesting of the energy bands at $E_L = 2.80$ eV, compared with 100% valley polarization at the K point ($E_L \sim 1.90$ eV) [50].

Now, let us discuss the case of bilayer MoS₂. In the case of bilayer MoS₂, we can observe interlayer vibration, which is called the shear and breathing modes shown in Fig. 1(b). As shown in Fig. 3(c), the helicity-exchange phenomenon for the Raman scattering occurs in the shear mode but does not occur in the breathing mode. This result is in good agreement with the experiment by Chen *et al.* [27]. Since bilayer MoS₂ has inversion symmetry, there is no valley polarization (σ_+ and σ_- light are equally absorbed at any k point), as shown in Fig. 4(b). That is a reason why the peak of the IMC mode is not enhanced at $E_L = 3.20$ eV [see Fig. 4(b)], in which the same situation should occur in the shear mode. Thus, the number of layers is a key factor in the occurrence of the interplay of valley polarization and the helicity-exchange phenomenon. The laser energy dependence of the Raman peak intensity for monolayer (bilayer) MoS₂ is expected to be similar to that for odd- (even-) layer MoS₂ because of the lack (existence) of inversion symmetry.

It should be mentioned that the Raman intensity of the IMC peak is comparable to that of the OC peak in the experiment [26,27], while our calculated results show that the IMC Raman peak is much weaker than the OC peak (almost $\frac{1}{20}$), which does not explain well the experiment quantitatively. One possible reason for the disagreement is the evaluation of γ in Eq. (1), which is related to the lifetime of the photoexcited carrier. The lifetime of the photoexcited carrier is different for the OC and IMC modes because of the valley polarization discussed in Fig. 5. In particular, the lifetime of the photoexcited carrier

for the Raman process of the IMC mode should be longer than that of the OC mode since the photoexcited carrier in the IMC Raman process cannot relax to the ground state by valley polarization, especially near the K (K') and Λ (Λ') points. Since the lifetime of the photoexcited carrier is evaluated by calculating the whole path of the electron-photon and electron-phonon scattering, it is beyond the present work. Within the simple analysis presented in the Supplemental Material [51], we calculated the Raman peak intensities of the IMC and OC modes using different γ for the IMC (γ_{IMC}) and OC (γ_{OC}) modes (see Fig. S3 in the Supplemental Material [51]). In this calculation, we found that the intensities of the IMC and OC modes become comparable when the values of γ_{IMC} and γ_{OC} are, respectively, 0.05 and 0.1 eV for $E_L = 3.20$ eV. Furthermore, Miranda *et al.* reported that the ratio of the Raman intensity for the IMC and OC modes in MoTe₂ is affected by the many-body effect and the exciton effect, which is calculated using the GW method with the Bethe-Salpeter equation [54]. According to the theoretical calculation by Miranda *et al.*, the exciton wave function makes the Raman intensities of the IMC and OC peaks more comparable, especially around the energy gap. Our calculation does not consider the many-body effect and uses a constant γ value. Thus, in this paper, we cannot discuss the ratio of the IMC and OC peaks using the exciton wave function, which should be a future problem. Nevertheless, it is highly desired that experimental work will check the E_L dependence of the relative Raman intensities between the IMC and OC modes.

C. Helicity-dependent Raman spectra of strained graphene

Finally, in order to understand the phenomenon and the relationship with the angular momentum of phonon, we calculate the Raman spectra of the G band under uniaxial strain. According to the discussion of conservation of angular momentum [26,35], the G band in graphene can change the helicity of the photon in the Raman process since the two modes

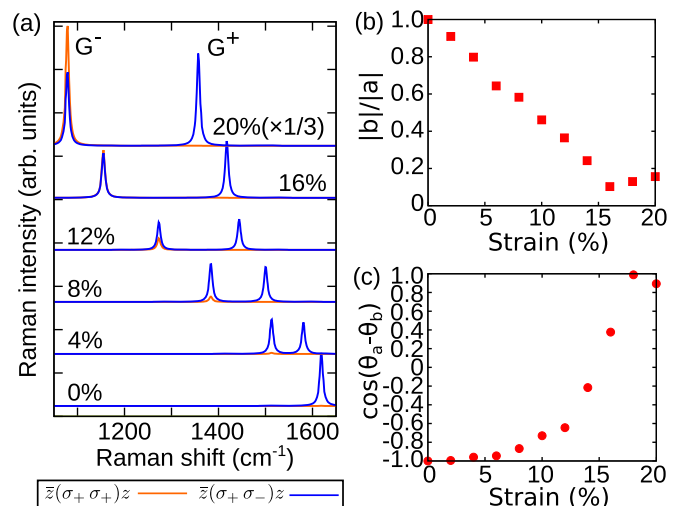


FIG. 6. (a) Calculated Raman spectra at $E_L = 2.0$ eV of strained graphene in the y direction in Fig. 1(a). The components (b) $|a/b|$ and (c) $\cos(\theta_a - \theta_b)$ in the Raman tensor of the G^- band as a function of strain.

(iTO and LO) are degenerate. Then, the helicity-selection rule would change if the degeneracy of the G band is lifted by applying uniaxial strain. Mohiuddin *et al.* and other researchers observed the splitting of the G band by 10 cm^{-1} through the application of 0.6% strain in graphene [36–38]. In Fig. 6(a), we show the calculated Raman spectra of the G band in graphene with the uniaxial strain in the direction of the y axis of Fig. 1(a). The G band splits into two bands (G^+ and G^-) by applying the strain, and the peak positions of the two peaks shift to the lower wave number. Because of the strain, the symmetry of graphene (D_{6h}) changes to D_{2h} , and the G band with E_{2g} symmetry splits into the A_g (G^-) and B_{1g} (G^+) symmetry modes. By increasing the strain, the Raman intensity of the G^- band for $\bar{z}(\sigma_+ \sigma_+)z$ becomes larger.

By using Eq. (6), we calculate the components of the Raman tensor from the first-principles calculation. Generally, the components of the Raman tensor are complex numbers since the matrix elements are complex numbers ($a = |a|e^{i\theta_a}$, $b = |b|e^{i\theta_b}$, and $c = |c|e^{i\theta_c}$). Then, the Raman intensity for the A_g symmetry is expressed by

$$I_{\sigma^+\sigma^+}^{A_g} = \left| \frac{a+b}{2} \right|^2 = \frac{|a|^2}{4} \left(1 + \left| \frac{b}{a} \right|^2 + 2 \left| \frac{b}{a} \right| \cos(\theta_a - \theta_b) \right), \quad (8)$$

$$I_{\sigma^-\sigma^+}^{A_g} = \left| \frac{a-b}{2} \right|^2 = \frac{|a|^2}{4} \left(1 + \left| \frac{b}{a} \right|^2 - 2 \left| \frac{b}{a} \right| \cos(\theta_a - \theta_b) \right). \quad (9)$$

In Figs. 6(b) and 6(c), we show the calculated $|b|/|a|$ and $\cos(\theta_a - \theta_b)$ as a function of strain. The Raman intensities for the helicity-changing and helicity-conserving cases at $\sim 16\%$ strain in Fig. 6 are almost the same since $\cos(\theta_a - \theta_b) \sim 0$ for 16% strain. Such strain dependences of a and b occur since the component b for the y direction in the Raman tensor \vec{R} (A_g) shown in Table I is modulated by the strain along the y direc-

tion. The Raman tensor for the B_{1g} mode is the same as that for the helicity-changing E' modes that the helicity changes in the Raman scattering process. Thus, the G^+ band in Fig. 6 changes the helicity and keeps the selection rule of helicity-dependent Raman spectra even though the strain increases.

Finally, let us comment on conservation of angular momentum for strained graphene. Our calculated results for the split G^+ and G^- bands exhibit changes in the helicity even though these modes are not degenerate. This result seems not to satisfy conservation of angular momentum. However, the crystal structures in the calculation do not have continuous rotational symmetry, and thus, the conservation of angular momentum is generally broken [55,56]. The angular momentum of photon might be changed to mechanical rotation of the system. Then the helicity-changing Raman spectra would be observed also in nondegenerate modes, and this behavior should be confirmed by additional experiments for materials such as black phosphorus, strained graphene, and other materials with D_{2h} symmetry.

IV. CONCLUSION

In conclusion, we have calculated the helicity-dependent first-order resonant Raman spectra of graphene and mono- and bilayer MoS_2 . The helicity-selection rule in Raman spectra is determined by the symmetry of phonons, while the valley polarization affects the laser energy dependence of the Raman intensity in the case of the IMC and OC phonon modes independently in monolayer MoS_2 . We also showed the helicity-dependent Raman spectra of the G band in strained graphene. The helicity-selection rule of the split G^- band changes to conserve the helicity with increasing strain, while the G^+ band does not change the helicity-selection rule.

ACKNOWLEDGMENTS

This work was supported by JSPS KAKENHI Grant No. JP25107005 and the World Premier International Research Center Initiative (WPI), MEXT, Japan.

-
- [1] K. S. Novoselov, A. K. Geim, S. V. Morozov, D. Jiang, Y. Zhang, S. V. Dubonos, I. V. Grigorieva, and A. A. Firsov, *Science* **306**, 666 (2004).
 - [2] W. Yang, J. Shang, J. Wang, X. Shen, B. Cao, N. Peimyoo, C. Zou, Y. Chen, Y. Wang, C. Cong *et al.*, *Nano Lett.* **16**, 1560 (2016).
 - [3] W. Yao, D. Xiao, and Q. Niu, *Phys. Rev. B* **77**, 235406 (2008).
 - [4] H.-Z. Lu, W. Yao, D. Xiao, and S.-Q. Shen, *Phys. Rev. Lett.* **110**, 016806 (2013).
 - [5] K. Y. Bliokh and F. Nori, *Phys. Rep.* **592**, 1 (2015).
 - [6] K. F. Mak, K. He, J. Shan, and T. F. Heinz, *Nat. Nanotechnol.* **7**, 494 (2012).
 - [7] K. F. Mak, K. He, C. Lee, G. H. Lee, J. Hone, T. F. Heinz, and J. Shan, *Nat. Mater.* **12**, 207 (2013).
 - [8] T. Cao, G. Wang, W. Han, H. Ye, C. Zhu, J. Shi, Q. Niu, P. Tan, E. Wang, B. Liu *et al.*, *Nat. Commun.* **3**, 887 (2012).
 - [9] H. Zeng, J. Dai, W. Yao, D. Xiao, and X. Cui, *Nat. Nanotechnol.* **7**, 490 (2012).
 - [10] A. M. Jones, H. Yu, N. J. Ghimire, S. Wu, G. Aivazian, J. S. Ross, B. Zhao, J. Yan, D. G. Mandrus, D. Xiao *et al.*, *Nat. Nanotechnol.* **8**, 634 (2013).
 - [11] S. Wu, J. S. Ross, G.-B. Liu, G. Aivazian, A. Jones, Z. Fei, W. Zhu, D. Xiao, W. Yao, D. Cobden *et al.*, *Nat. Phys.* **9**, 149 (2013).
 - [12] R. Suzuki, M. Sakano, Y. J. Zhang, R. Akashi, D. Morikawa, A. Harasawa, K. Yaji, K. Kuroda, K. Miyamoto, T. Okuda *et al.*, *Nat. Nanotechnol.* **9**, 611 (2014).
 - [13] W.-T. Hsu, Y.-L. Chen, C.-H. Chen, P.-S. Liu, T.-H. Hou, L.-J. Li, and W.-H. Chang, *Nat. Commun.* **6**, 8963 (2015).
 - [14] T. Yan, X. Qiao, P. Tan, and X. Zhang, *Sci. Rep.* **5**, 15625 (2015).
 - [15] G. Aivazian, Z. Gong, A. M. Jones, R.-L. Chu, J. Yan, D. G. Mandrus, C. Zhang, D. Cobden, W. Yao, and X. Xu, *Nat. Phys.* **11**, 148 (2015).

- [16] K. Hao, G. Moody, F. Wu, C. K. Dass, L. Xu, C.-H. Chen, L. Sun, M.-Y. Li, L.-J. Li, A. H. MacDonald *et al.*, *Nat. Phys.* **12**, 677 (2016).
- [17] J. Huang, T. B. Hoang, and M. H. Mikkelsen, *Sci. Rep.* **6**, 22414 (2016).
- [18] T. Smoleński, M. Goryca, M. Koperski, C. Faugeras, T. Kazimierczuk, A. Bogucki, K. Nogajewski, P. Kossacki, and M. Potemski, *Phys. Rev. X* **6**, 021024 (2016).
- [19] E. J. Sie, J. W. McIver, Y.-H. Lee, L. Fu, J. Kong, and N. Gedik, *Nat. Mater.* **14**, 290 (2015).
- [20] Y. J. Zhang, T. Oka, R. Suzuki, J. T. Ye, and Y. Iwasa, *Science* **344**, 725 (2014).
- [21] L. Malard, M. Pimenta, G. Dresselhaus, and M. Dresselhaus, *Phys. Rep.* **473**, 51 (2009).
- [22] R. Saito, M. Hofmann, G. Dresselhaus, A. Jorio, and M. S. Dresselhaus, *Adv. Phys.* **60**, 413 (2011).
- [23] R. Saito, Y. Tatsumi, S. Huang, X. Ling, and M. S. Dresselhaus, *J. Phys. Condens. Matter* **28**, 353002 (2016).
- [24] C. Cong, T. Yu, K. Sato, J. Shang, R. Saito, G. F. Dresselhaus, and M. S. Dresselhaus, *ACS Nano* **5**, 8760 (2011).
- [25] P. H. Tan, W. P. Han, W. J. Zhao, Z. H. Wu, K. Chang, H. Wang, Y. F. Wang, N. Bonini, N. Marzari, N. Pugno *et al.*, *Nat. Mater.* **11**, 294 (2012).
- [26] S. G. Drapcho, J. Kim, X. Hong, C. Jin, S. Shi, S. Tongay, J. Wu, and F. Wang, *Phys. Rev. B* **95**, 165417 (2017).
- [27] S.-Y. Chen, C. Zheng, M. S. Fuhrer, and J. Yan, *Nano Lett.* **15**, 2526 (2015).
- [28] C. Lee, H. Yan, L. E. Brus, T. F. Heinz, J. Hone, and S. Ryu, *ACS Nano* **4**, 2695 (2010).
- [29] S.-L. Li, H. Miyazaki, H. Song, H. Kuramochi, S. Nakaharai, and K. Tsukagoshi, *ACS Nano* **6**, 7381 (2012).
- [30] H. Li, Q. Zhang, C. C. R. Yap, B. K. Tay, T. H. T. Edwin, A. Olivier, and D. Baillargeat, *Adv. Funct. Mater.* **22**, 1385 (2012).
- [31] L. Sun, J. Yan, D. Zhan, L. Liu, H. Hu, H. Li, B. K. Tay, J.-L. Kuo, C.-C. Huang, D. W. Hewak *et al.*, *Phys. Rev. Lett.* **111**, 126801 (2013).
- [32] H.-L. Liu, H. Guo, T. Yang, Z. Zhang, Y. Kumamoto, C.-C. Shen, Y.-T. Hsu, L.-J. Li, R. Saito, and S. Kawata, *Phys. Chem. Chem. Phys.* **17**, 14561 (2015).
- [33] M. A. Pimenta, E. del Corro, B. R. Carvalho, C. Fantini, and L. M. Malard, *Acc. Chem. Res.* **48**, 41 (2015).
- [34] L. Zhang and Q. Niu, *Phys. Rev. Lett.* **112**, 085503 (2014).
- [35] L. Zhang and Q. Niu, *Phys. Rev. Lett.* **115**, 115502 (2015).
- [36] T. M. G. Mohiuddin, A. Lombardo, R. R. Nair, A. Bonetti, G. Savini, R. Jalil, N. Bonini, D. M. Basko, C. Galiotis, N. Marzari *et al.*, *Phys. Rev. B* **79**, 205433 (2009).
- [37] M. Huang, H. Yan, C. Chen, D. Song, T. F. Heinz, and J. Hone, *Proc. Natl. Acad. Sci. USA* **106**, 7304 (2009).
- [38] O. Frank, G. Tsoukleri, J. Parthenios, K. Papagelis, I. Riaz, R. Jalil, K. S. Novoselov, and C. Galiotis, *ACS Nano* **4**, 3131 (2010).
- [39] A. Jorio, M. S. Dresselhaus, R. Saito, and G. Dresselhaus, *Raman Spectroscopy in Graphene-Related Systems* (Wiley, New York, 2011).
- [40] B. R. Carvalho, L. M. Malard, J. M. Alves, C. Fantini, and M. A. Pimenta, *Phys. Rev. Lett.* **114**, 136403 (2015).
- [41] J. J. Sakurai, *Modern Quantum Mechanics*, 2nd ed. (Addison-Wesley, Boston, 2011).
- [42] A. Grüneis, R. Saito, G. G. Samsonidze, T. Kimura, M. A. Pimenta, A. Jorio, A. G. Souza Filho, G. Dresselhaus, and M. S. Dresselhaus, *Phys. Rev. B* **67**, 165402 (2003).
- [43] J. Noffsinger, F. Giustino, B. D. Malone, C.-H. Park, S. G. Louie, and M. L. Cohen, *Comput. Phys. Commun.* **181**, 2140 (2010).
- [44] S. Ponce, E. R. Margine, C. Verdi, and F. Giustino, *Comput. Phys. Commun.* **209**, 116 (2016).
- [45] F. Giustino, M. L. Cohen, and S. G. Louie, *Phys. Rev. B* **76**, 165108 (2007).
- [46] P. Giannozzi, S. Baroni, N. Bonini, M. Calandra, R. Car, C. Cavazzoni, D. Ceresoli, G. L. Chiarotti, M. Cococcioni, I. Dabo *et al.*, *J. Phys. Condens. Matter* **21**, 395502 (2009).
- [47] H. J. Monkhorst and J. D. Pack, *Phys. Rev. B* **13**, 5188 (1976).
- [48] S. Baroni, S. de Gironcoli, A. D. Corso, and P. Giannozzi, *Rev. Mod. Phys.* **73**, 515 (2001).
- [49] K. F. Mak, C. Lee, J. Hone, J. Shan, and T. F. Heinz, *Phys. Rev. Lett.* **105**, 136805 (2010).
- [50] Y. Tatsumi, K. Ghalamkari, and R. Saito, *Phys. Rev. B* **94**, 235408 (2016).
- [51] See Supplemental Material at <http://link.aps.org/supplemental/10.1103/PhysRevB.97.115407> for the details of electron-photon, electron-phonon, and Raman matrix elements displayed in the Brillouin zone, group theory analysis to give the selection rule of the helicity-dependent Raman spectra, and a simple analysis of the different broadening factors γ for the OC and IMC modes to give the resonance condition of the Raman intensity.
- [52] A. Carvalho, R. M. Ribeiro, and A. H. Castro Neto, *Phys. Rev. B* **88**, 115205 (2013).
- [53] D. Kozawa, R. Kumar, A. Carvalho, K. K. Amara, W. Zhao, S. Wang, M. Toh, R. M. Ribeiro, A. H. C. Neto, K. Matsuda *et al.*, *Nat. Commun.* **5**, 4543 (2014).
- [54] H. P. C. Miranda, S. Reichardt, G. Froehlicher, A. Molina-Sanchez, S. Berciaud, and L. Wirtz, *Nano Lett.* **17**, 2381 (2017).
- [55] J. Visser, E. R. Eliel, and G. Nienhuis, *Phys. Rev. A* **66**, 033814 (2002).
- [56] T. Higuchi, N. Kanda, H. Tamaru, and M. Kuwata-Gonokami, *Phys. Rev. Lett.* **106**, 047401 (2011).